

See discussions, stats, and author profiles for this publication at: <https://www.researchgate.net/publication/233390474>

Gold Branched Nanoparticles for Cellular Treatments

ARTICLE *in* THE JOURNAL OF PHYSICAL CHEMISTRY C · AUGUST 2012

Impact Factor: 4.77 · DOI: 10.1021/jp305021k

CITATIONS

21

READS

82

14 AUTHORS, INCLUDING:



Maurizio Gaultieri

ENEA

58 PUBLICATIONS 788 CITATIONS

[SEE PROFILE](#)



Laura D'Alfonso

Università degli Studi di Milano-Bicocca

57 PUBLICATIONS 716 CITATIONS

[SEE PROFILE](#)



Maddalena Collini

Università degli Studi di Milano-Bicocca

79 PUBLICATIONS 1,196 CITATIONS

[SEE PROFILE](#)



Giuseppe Chirico

Università degli Studi di Milano-Bicocca

140 PUBLICATIONS 2,079 CITATIONS

[SEE PROFILE](#)

Gold Branched Nanoparticles for Cellular Treatments

Laura Sironi,[†] Stefano Freddi,[†] Michele Caccia,[†] Paolo Pozzi,[†] Leone Rossetti,[†] Piersandro Pallavicini,*[‡]
Alice Donà,[‡] Elisa Cabrini,[‡] Maurizio Gualtieri,[§] Ilaria Rivolta,^{||} Alice Panariti,^{||} Laura D'Alfonso,[†]
Maddalena Collini,[†] and Giuseppe Chirico*,[†]

[†]Physics Department, Università degli Studi di Milano Bicocca, Piazza della Scienza 3, I-20126 Milano, Italy

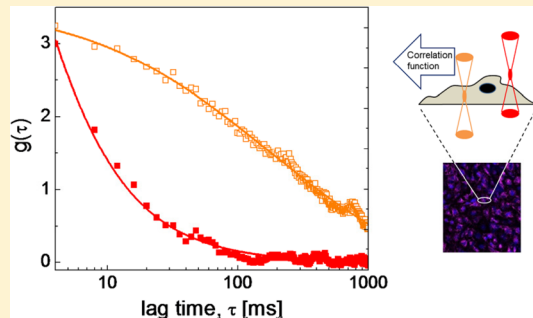
[‡]General Chemistry Department, Università degli studi di Pavia, Pavia, Italy

[§]Ambiental Science Department, Università degli Studi di Milano Bicocca, Piazza della Scienza 2, I-20126 Milano, Italy

^{||}Experimental Medicine Department, Università degli Studi di Milano Bicocca, via Cadore 8, 20052 Monza, Italy

S Supporting Information

ABSTRACT: Under the action of near-infrared radiation, shape anisotropic gold nanoparticles emit two-photon luminescence and release heat. Accordingly, they have been proposed for imaging, photothermal therapies and thermo-controlled drug delivery. In all these applications particular care must be given to control the nanoparticle – cell interaction and the thermal efficiency of the nanoparticles, while minimizing their intrinsic cytotoxicity. We present here the characterization of the cell interaction of newly developed branched gold nanostars, obtained by laurylsulfobetaine-driven seed-growth synthesis. The study provides information on the size distribution, the shape anisotropy, the cellular uptake and cytotoxicity of the gold nanostars as well as their intracellular dynamic behavior by means of two-photon luminescence imaging, fluorescence correlation spectroscopy and particle tracking. The results show that the gold nanostars are internalized as well as the widely used gold nanorods and are less toxic under prolonged treatments. At the same time they display remarkable two-photon luminescence and large extinction under polarized light in the near-infrared region of the spectrum, 800–950 nm. Gold nanostars appear then a valuable alternative to other elongated or in-homogeneous nanoparticles for cell imaging.



INTRODUCTION

Metal and oxide nanoparticles (NPs) have many applications in biology, medicine,^{1–5} and nanobiotechnology^{6–9} in terms of imaging,^{3,4} diagnosis,⁵ and therapy,^{2,3} owing to the combination of their shape and size-dependent light extinction^{10,11} with stability and low cytotoxicity.¹² Gold nanorods (GNRs)^{13,14} and non spherically symmetric gold NPs in general, such as gold nanostars (GNSs) and nanocages,^{15–18} have additional valuable properties for applications in biochemical sensing, diagnostics,^{19–21} and medical therapy.^{3,21,22,13} In fact, their surface plasmon resonance (SPR) can be tuned from the visible to the near-infrared (NIR) region by increasing the aspect ratio of gold nanorods, the aspect ratio of the nanostar branches, or the shell thickness of the nanocages.^{1,17,23}

SPR extinction spectra of gold anisotropic or nonspherically symmetric nanostructures include contributions from scattering and absorption, whose balance depends on their shape and size.^{24,25} The absorption is responsible for a substantial thermal load^{1,13,14,26} and for intrinsic two-photon luminescence^{3,4,27–29} that is much larger than one photon fluorescence.³⁰ GNRs, the reference nonspherical gold NPs, display, in addition to the standard SPR mode (at 520–550 nm), a less energetic SPR band resonance^{31,32} that can be tuned from the red to the near-infrared region by increasing their aspect ratio. These

spectroscopic properties have been exploited in optical microscopy of cancer cells (through scattering),¹⁴ in localized hyperthermia of cancer cells,^{22,13,26,1,2,33} or in combined treatments of cancers,³⁴ since nonspherically symmetric and anisotropic gold NPs can, in general, efficiently convert optical energy into heat via nonradiative electron relaxation dynamics.^{26,35,17}

The possibility of nanoparticle-based cell therapies is largely dependent on the shape and surface charge of the nanoparticles. Cationic NPs are known to interact strongly with the negative cell membrane, with a maximum of internalization efficiency at size $\cong 50$ nm.^{36,37} However, the fast and efficient internalization of very small (size ≤ 20 nm) cationic gold nanoparticles occurs through direct membrane pores in lipid bilayers and might then lead to a permanent damage of the cell membrane and to cell death.²⁵ Negatively charged NPs are instead slowly taken up by cells with endocytosis or pinocytosis mechanisms.^{25,38} Also, the shape has a very strong influence on the NP internalization, since spherically symmetric NPs are

Received: May 23, 2012

Revised: July 31, 2012

Published: August 2, 2012



500% more efficiently uploaded by the cell with respect to rodlike ones.³⁷

The most popular method for synthesizing GNRs involves the seed-mediated approach based on the use of the cationic cetyltrimethylammonium bromide (CTAB) surfactant as the protecting and shape-directing agent.^{15,32,39} GNRs prepared in this way display positive surface charge due to a strongly bound interdigitated double layer of CTAB molecules grafted to their surface.⁴⁰ We have recently reported the synthesis of branched gold nanoparticles obtained by seed growth synthesis with the zwitterionic surfactant laurylsulphobetaine (LSB). Notably, LSB concentration permits controlling the size of the NPs and the SPR position that can be tuned into the 700–1100 nm NIR spectral range.²³ The GNSs have an overall negative surface charge (ζ -potential = −15 mV) due to the LSB molecules forming a double layer on the GNS surface and presenting sulfate moieties to the solvent interface.²³ Moreover, branched gold nano-objects have also been recently demonstrated to efficiently convert into heat the radiation absorbed on their SPR maximum.^{41,42}

We argue here that, since the shape has a large influence on the internalization,^{25,36,37} the adoption of a highly branched nanostructure might keep the internalization efficiency high, making these objects useful alternatives to gold nanorods in cell imaging and photothermal therapies. In order to ascertain this hypothesis, we carried out a detailed comparative spectroscopic characterization of the response of the gold nanorods and nanostars to NIR radiation, also in terms of nonlinear luminescence, intrinsic brightness and polarization response. We also examined and compared the possibility of using either the GNRs or the GNSs as staining agents in cell imaging. To this purpose we studied the interaction of the GNSs with the cells by fluorescence two-photon microscopy and characterized their intracellular behavior by particle tracking and fluorescence correlation spectroscopy.

■ EXPERIMENTAL METHODS

Nanoparticles Synthesis. Gold nanoparticles CTAB seed growth was obtained as described previously by El-Sayed³⁹ and LSB seed growth was obtained as described previously by us²³ (see also Supporting Information for the conditions chosen for the GNRs preparations). Pegylated gold NPs were obtained by centrifuging (13,000 rpm for 20 min) the suspensions and recovering and redissolving the pellet in 10 mL of bidistilled water. The dispersion was then treated with 1.0–1.1 mg of PEG₂₀₀₀SH polymer (Iris Biotech, MeO-PEG-SH, MW = 2000 Dalton), corresponding to $\approx 1:10$ Au/PEG₂₀₀₀SH molar ratio, with respect to the total starting Au moles.²³

Gold content was determined with the following protocol: after the growth process, the solutions were centrifuged, the supernatant was removed, and the pellet of nanoparticles was suspended in the same volume as before centrifugation. Ionic gold and not-grown seeds are thus removed. Two milliliters of the obtained solution was treated with 400 μ L of freshly prepared aqua regia, observing immediate oxidation. Each sample was then diluted 1:20 with bidistilled water and analyzed at ICP-OES to determine the Au content. Data were collected with an ICP-OES OPTIMA 3000 Perkin-Elmer instrument. Data were in the range of 0.07 mg Au/mL and 0.03 mg Au/mL for nanostars and nanorods, respectively.

ζ -Potential Characterization. The gold nanorods ([CTAB] = 0.2 M) have a slightly positive ζ -potential, ζ = 14.0 \pm 10.5 mV. The GNSs are characterized by moderate

negative values of the ζ -potential: ζ = −27 \pm 6 mV ([LSB] = 0.3 M) and ζ = −13.4 \pm 4.5 mV ([LSB] = 0.45 M). These values indicate that all the NPs used here have a prevalent negative surface charge in a moderately stable condition.

Cell Culture. Cellular uptake experiments have been performed on A549, HeLa, and HEK293 cells. Twenty-four hours before the experiments, 10⁶ cells per well have been plated on six-well tissue plates in Dulbecco's modified Eagle's Medium (DMEM) supplemented with 10% heat-inactivated fetal bovine serum, 2 mM L-glutamine, penicillin–streptomycin (EuroClone), at 37 °C in a 5% CO₂ atmosphere. For fluorescence correlation measurement in living cells, the culture medium (10% FBS) has been replaced with a diluted medium (1% FBS) 30 min before the beginning of the measurements in order to reduce the aggregation of the nanoparticles.

In the MTT cell viability assay, MTT [3-(4,5-dimethylthiazol-2-yl)-2,5-diphenyl tetrazolium bromide] was used to test cytotoxicity of reagents and cell viability. The MTT reduced by the metabolically active cells to insoluble purple formazan dye crystals was then detected through its absorbance at 570 nm, after being solubilized in DMSO.

For the quantification of the internalization of GNRs and GNSs the cells were plated on glass coverslips and, at confluence, they were incubated with the GNRs or the GNSs. After 4 or 24 h of treatment, cells were fixed with 4% paraformaldehyde in PBS at room temperature for 20 min. Cells were washed three times in PBS. DAPI was used to stain cell nuclei at a concentration of 1 μ M in PBS for 5 min. Coverslips were mounted with glycerol.

Spectral Characterization. Spectrophotometric measurements of the suspensions were performed on a Jasco V570 spectrophotometer (Jasco, Japan).

Dynamic Light-Scattering Characterization. The dynamic light scattering (DLS) measurements of the scattered light were performed on a homemade setup as a function of the scattering angles and the light polarization (source: polarized He–Ne laser, 30 mW output power, vertically polarized). The emission is collected through a Glan Thomson polarizer set parallel (configuration VV) or perpendicular (configuration VH) to the exciting polarization. The correlator board was an ISS (Urbana–Champaign, IL) single photon counting acquisition board. The intensity AutoCorrelation Function (ACF) was fit to the trial function:⁴³

$$G(t) = \langle I \rangle^2 (1 + f^2 |g^{(1)}(t)|^2) \quad (1)$$

where $g^{(1)}(\tau)$ is the field ACF, taken in general as the sum of exponential decays. For spherically symmetric particles, the field ACF, $g^{(1)}(t)$, is described by a single exponential relaxation whose rate is related to the translational diffusion coefficient, D , and the scattering vector, Q , as $D = \Gamma/Q^2$. The scattering vector $Q = [4\pi n \sin(\theta/2)]/\lambda$ is computed from the water index of refraction, $n = 1.33$, the scattering angle, θ , and the laser wavelength, $\lambda = 633$ nm.

The polarizability of the particle is, in general, a rank two tensor and can be diagonalized to give three eigenvalues that measure the polarizability along three orthogonal axes in the particle frame of reference. For the sake of simplicity, we assume cylindrical symmetry for the NPs with axial polarizability, $\alpha_{||}$, which is much larger than the transverse one, α_{\perp} . Within this assumption, the intensity autocorrelation function can be written in the form:⁴³

$$\begin{aligned} g_{VV}^{(1)}(\tau) &= \exp[-2\tau DQ^2](1 + \mathcal{R} \exp[-\tau 6\Theta]) \\ &= \exp[-\tau/\tau_T] + \mathcal{R} \exp[-\tau/\tau_R] \\ g_{VH}^{(1)}(\tau) &= \exp[-2\tau DQ^2] \exp[-\tau 6\Theta] = \exp[-\tau/\tau_R] \end{aligned} \quad (2)$$

where \mathcal{R} is the depolarization ratio:

$$\mathcal{R} = \frac{4}{45} \frac{(\alpha_{||} + \alpha_{\perp})^2}{\langle \alpha \rangle^2} = \frac{4}{45} \frac{\delta \alpha^2}{\langle \alpha \rangle^2}$$

and D and Θ are the translational and tumbling rotational diffusion coefficients, respectively. Due to the fast tumbling motion, gold nanostars can be considered to behave as isotropic nanoparticles. In this case the translational and rotational diffusion coefficients are related to the hydrodynamic radius, R_h , as:

$$\left\{ \begin{array}{l} D = \frac{K_B T}{6\pi\eta R_{h,T}} \\ \Theta = \frac{K_B T}{8\pi\eta R_{h,R}^3} \end{array} \right. \quad (3)$$

In eq 3 K_B is the Boltzmann constant, and the suspension viscosity, η , is taken equal to the solvent viscosity due to the extremely low volume fraction of the suspensions. For gold nanorods that have a clear cylindrical symmetry one should instead use corrections to eq 3 in terms of the axial ratio of the NP, as discussed by Tirado and Garcia de la Torre:⁴⁴

$$\begin{aligned} D_{TG} &= D_0[\ln(AR) + \sigma_T] \\ \sigma_T &= 0.312 + \frac{0.565}{AR} + \left(\frac{0.316}{AR} \right)^2 \\ \Theta_{TG} &= \Theta_0[\ln(AR) + \sigma_R] \\ \sigma_R &= -0.662 + \frac{0.917}{AR} - 0.05 \left(\frac{0.917}{AR} \right)^2 \end{aligned} \quad (4)$$

where $AR = L/d$ and Θ_0 and D_0 are the limiting values, $D_0 = K_B T (3\pi\eta L)^{-1}$ and $\Theta_0 = 3K_B T (3\pi\eta L^3)^{-1}$.

The contribution of LSB micelles to the ACFs was found to be negligible: pure LSB solutions revealed spherical micelles with diameters increasing from 1.6 ± 0.2 nm to 3.0 ± 0.3 nm when increasing the LSB concentration from 0.2 to 0.6 M.²³

Fluorescence Correlation Spectroscopy. We implemented FCS experiments in suspensions on a homemade setup described elsewhere.⁴⁵ A pseudo-cross-correlation acquisition mode of the ACFs of the fluorescence fluctuations, primed by two-photon excitation, was implemented⁴⁶ by splitting two replicas of the polarized TPL signal on two distinct detectors and by computing the cross-correlation of the two channels. The fluorescence from rhodamine 6G and gold nanoparticles was selected by band-pass filters at 560 nm (Chroma Inc., Brattleboro, VT, HQ560/40) and at 535 nm (Chroma Inc., Brattleboro, VT, HQ535/50), respectively. The ACFs were acquired by two identical detectors, and the normalized ACFs and cross-correlation functions were computed by an ALV5000E (ALV, Langen, D) board.

The analytical form of this cross-correlation function is the superposition of the rotational (double exponential) component to the translational diffusion hyperbolic decay.^{47,48}

$$g(t) = g(0) \left[1 + A_{R1} \exp\left(-\frac{10}{3} \frac{t}{\tau_R}\right) + A_{R2} \exp(-t/\tau_D) \right] \left[1 + \frac{t}{\tau_D} \right]^{-1} \left[1 + \frac{t}{S^2 \tau_D} \right]^{-0.5} \quad (5)$$

In eq 5 the relaxation times are τ_D and τ_R that are related to the translational and the tumbling rotational diffusion coefficients, D and Θ , respectively, by the relations:

$$\left\{ \begin{array}{l} \tau_D = \frac{\omega_0^2}{8D} \\ \tau_R = (6\Theta)^{-1} \end{array} \right. \quad (6)$$

The laser beam waist is ω_0 , and the structure factor S (here assumed $S = 5$) is the ratio between the $x - y$ and z extension of the point spread function. The beam waist measured from the diffusion time of rhodamine 6G in ethanol solutions is $\omega_0 = 0.6 - 0.76 \mu\text{m}$, and it corresponds to an axial resolution of $1.4 - 2.2 \mu\text{m}$.

The zero lag time extrapolation of the correlation function, $g(0)$ in eq 5, provided a direct estimate of the number of luminescent NPs in the excitation volume, $V_{\text{exc}} = \pi\omega_0^4/\lambda$, through the relation⁴⁹ $\langle N \rangle = \gamma/g(0)$, where γ is a geometrical factor depending on the shape of the excitation laser mode; here $\gamma = 0.076$.⁵⁰

The TPL emission spectra were recorded by means of a CCD (DV420A-BV, Andor, IRL)-based spectrometer (MS125, Lot-Oriel, UK), connected to the back port of the microscope. The excitation wavelength is variable in the range 730–920 nm with a constant average power on the sample of about 2 mW. Each spectrum is the result of the accumulation of 10–20 acquisitions of 1 s duration.

Fluorescence Microscopy. The two-photon excitation fluorescence time-lapse imaging was performed on a confocal scanning microscope (BX51 equipped with FV300, Olympus, Japan) modified for direct (non-descanned) detection of the signal⁵¹ and coupled to a femtosecond Ti:sapphire laser (Mai Tai, Spectra Physics, CA). The microscope was equipped with a highly efficient water immersion objective (N.A. = 0.95, 20×, water immersion, Olympus, Japan), and the TPL emission was filtered through a short-pass 670 nm filter (Chroma Inc., Brattleboro, VT) and selected by a band-pass filter at 535 nm (Chroma Inc., Brattleboro, VT, HQ535/50).

For TPL polarization measurements, images were obtained by averaging three images collected through an HQ535/50 band-pass filter, and no analyzer was used. The TPL signal was measured by summing the pixel content over regions of interest (ROIs) taken around single bright spots ascribed to isolated particles, as judged from the emission level of the single spot with respect to the distribution of levels computed on a full frame.

For intracellular FCS experiments we employed a Cascade II:512 Photometrics EM-CCD camera (Photometrics, Tucson, AZ) coupled to the top camera port of the BX51 Olympus microscope. We typically acquired time series of 30,000 images ($20 \times 20 \mu\text{m}^2$) from single cells at a frame rate of 250 Hz (4 ms per frame). In order to monitor online the nanoparticle

behavior right outside and inside the cells, we split the laser beam by means of a Tweman-Green interferometer, thereby obtaining two equal intensity spots on the focal plane. The correlation function was then computed on each of the two spots and fit to a general functional form that can take into account anomalous diffusion and drift motion of the luminescent particles:^{52,53}

$$g_{AD}(t) = \frac{g(0)}{\left[1 + \left(\frac{t}{\tau_D}\right)^\alpha\right] \left[1 + \frac{t}{s^2 \tau_D}\right]^{-0.5}} \exp\left[-\left(\frac{t}{\tau_V}\right)^2\right] \quad (7)$$

In eq 7 τ_V is the drift correlation time that represents the time needed by a particle with drift velocity (V in modulus) to cross the beam waist whose size is ω_0 : $\tau_V = \omega_0/V$. It must be noted that eq 7 is an approximation of the more complete function:^{52,53} in the limit $\tau_D \ll \tau_V$.

Particle Tracking. The tracking of the luminescent organelles observed in the cells treated with the gold nanoparticles was performed by acquiring 50 images in time-lapse mode at an image sampling time of 800 ms with an Olympus confocal microscope adapted for two-photon excitation. The time series of images were analyzed with the tracking software Imaris (BITPLANE, Zurich, CH), the luminescent organelles were segmented and followed along the time series of images. All the tracking was performed on two dimensional (2D) images.

RESULTS AND DISCUSSION

The gold nanorods were obtained by CTAB-mediated seed growth^{23,54} according to a literature protocol³⁹ (see Supporting Information [SI], section 1, for synthetic details). They have defined the aspect ratio (Table S1, SI) that may differ slightly from batch to batch ($2.8 \leq \text{axial ratio} \leq 3.7$). We also prepared pegylated gold nanorods by addition of excess PEG₂₀₀₀SH to aqueous solutions of the gold nanorods, according to a procedure described in the literature⁵⁵ (see the Experimental Methods).

The synthesis of the gold nanoparticles obtained by LSB-directed seed growth has been reported by us elsewhere.²³ They display three distinct structures²³ (Figure 1 and Figures S1–2, SI): spherically symmetric NPs (less abundant population indicated as “A” in Figure 1A) and two populations of branched structures with intermediate (indicated as “B” in Figure 1A) or high axial ratio (indicated as “C” in Figure 1A) branches (Figure S2, SI).²³ We collectively call these structures gold nanostars (GNSs). Due to the weak nature of the LSB–gold interaction, all the GNSs populations can be easily coated with PEG₂₀₀₀SH by simple addition of an excess of the thiolated polymer to their aqueous solutions.²³ The typical structure of the gold nanorods is shown in Figure 1B for reference.

The extinction spectrum of the gold nanorods has two major components in the vis–NIR range (Figure 1C, solid line) that are due to surface plasmon resonances (SPRs).^{10,24,39,54} The shorter wavelength SPR falls at $\lambda \cong 520$ nm, close to that reported for gold nanospheres, and the two spectral components of the GNRs correspond to the SPR parallel and perpendicular to the rod axis.^{24,11} The extinction spectra of the gold nanostars synthesized with $0.2 \text{ M} \leq [\text{LSB}] \leq 0.6 \text{ M}$ are shown in Figure 1C ([dash], [dot], and [dot-dot-dash], increasing [LSB]). In this case three bands in the UV–vis extinction spectrum that are correlated to the three different NPs populations can be singled out.²³ Also in this case we

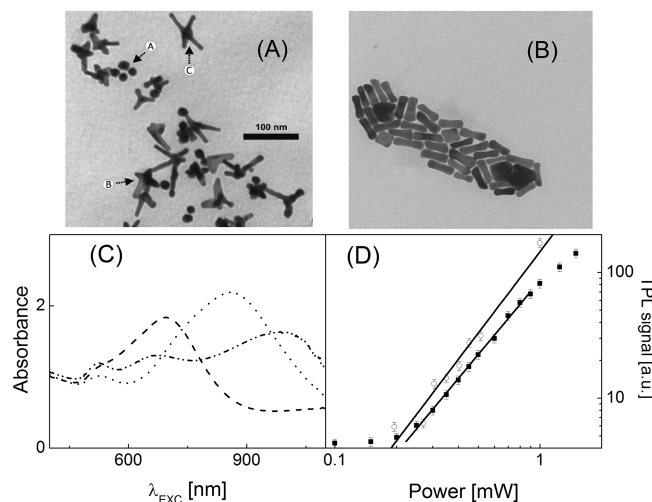


Figure 1. (A) TEM image of a sample grown at $[\text{LSB}] = 0.45 \text{ M}$. The structures indicated by the letters A, B, and C in the image indicate the spherical and the low and the high axial ratio nanostars, respectively. (B) TEM image of a sample grown at $[\text{CTAB}] = 0.20 \text{ M}$ showing the nanorods structure. (C) UV–vis spectra of the gold nanorods ($[\text{CTAB}] = 0.2 \text{ M}$, solid line) and of gold nanostars ($[\text{LSB}] = 0.2 \text{ M}$, dash line; 0.35 M , dot line; and 0.45 M , dot-dot-dash line). (D) Quadratic dependence of the signal intensity I_{TPL} on the excitation power for samples obtained with $[\text{CTAB}] = 0.2 \text{ M}$ (open circles) and $[\text{LSB}] = 0.45 \text{ M}$ (solid squares). The solid lines are the best fit to the power law $I_{\text{TPL}} \propto P_{\text{exc}}^\epsilon$, with $\epsilon = 2.1 \pm 0.2$ and $\epsilon = 1.95 \pm 0.04$ for the gold nanorods and the gold nanostars, respectively.

observe a short wavelength resonance that closely resembles that of spherical gold nanoparticles and is ascribed to the residual A population (Figure 1A). The intermediate (Figure 1C, [dot], $\lambda \cong 850 \text{ nm}$) and the long wavelength (Figure 1C, [dot-dot-dash], $\lambda \cong 950 \text{ nm}$) resonances are instead ascribed to the B and C population (Figure 1A), respectively.²³ The NIR component, whose position depends on the LSB concentration (Figure S3, SI), is largely responsible for the thermal release in the medium and can be exploited for photothermal applications, as indicated by the behavior of similar gold nano-objects^{41,42} and by our preliminary results. Briefly, GNSs and high aspect ratio GNRs suspensions (Au concentrations $\cong 0.1 \text{ mg/mL}$), irradiated by a near-infrared laser ($\lambda = 800 \text{ nm}$, power 200 mW), showed similar increments of the suspension temperature ($\Delta T \cong 18\text{--}22^\circ\text{C}$) above the room conditions. Further details will be given in a publication in preparation.

Information on the size and shape of the nanoparticles in the growth solutions can be gained from the analysis of the polarized and depolarized scattered light AutoCorrelation Functions (ACFs, eq 1).^{43,56} All the scattering ACFs were analyzed as the sum of two exponential relaxations with characteristic decay times $\tau_T \cong 150\text{--}200 \mu\text{s}$ and $\tau_R \cong 5\text{--}15 \mu\text{s}$ (see eq 2). The amplitude of the slower component was substantially reduced in the depolarized light ACF ($g_{VV}^{(1)}(\tau)$ in eq 2) and both were needed to fit the trend of ACFs collected under polarized light ($g_{VV}^{(1)}(\tau)$ in eq 2). Therefore we ascribed the two components to the translational and the rotational diffusion of the GNRs and GNSs.⁴³ From the best fit of the $g_{VV}^{(1)}(\tau)$ correlation function to eq 2, we obtained the translational, D , and the rotational, Θ , diffusion coefficients.

The value of the average rotational tumbling diffusion coefficient for the GNRs suspensions lies in the ranges $20 \leq \Theta \leq 45 \text{ kHz}$ (see Table 1). We can predict very similar values by

Table 1. Structural Data Obtained from Dynamic Light Scattering and Fluorescence Correlation Spectroscopy, Compared to Those Obtained from Transmission Electron Microscopy (TEM subscript)^a

		Polarized Scattering ACFs			
[seed growth surfactant]	(<i>L/d</i>) _{TEM}	Θ_{exp} [kHz]	Θ_{TG} [kHz]	L_{TEM} [nm]	
0.2 M	CTAB	2.8 ± 0.3	22 ± 0.4	23 ± 3	48 ± 4
0.2 M ^b	CTAB	3.7 ± 0.9	43 ± 1.2	46 ± 13	42 ± 3
[seed growth surfactant]	$R_{\text{h,T}}$ [nm]	$R_{\text{h,R}}$ [nm]	\mathcal{R}	$(L/B)_{\text{TEM}}$	
0.2 M	LSB	24 ± 2	21 ± 3	1.8 ± 0.2	5 ± 2
0.35 M	LSB	29 ± 2	28 ± 4	1.9 ± 0.2	6 ± 2
0.45 M	LSB	21 ± 3	27 ± 3	2.2 ± 0.3	6 ± 2
Fluorescence ACFs					
[seed growth surfactant]	Θ_{FCS} [kHz]	Θ_{TG} [kHz]	R_{eff} [nm]	R_{eff} [nm]	conc [nM]
0.2 M	CTAB	21 ± 2	23 ± 3	18 ± 5	0.25 ± 0.03
0.2 M ^b	CTAB	40 ± 4	46 ± 13		0.26 ± 0.03
0.2 M	LSB	8 ± 1		34 ± 2	0.3 ± 0.03
0.35 M ^b	LSB	6 ± 2		45 ± 3	0.05 ± 0.01
0.45 M	LSB	9 ± 1		67 ± 4	0.18 ± 0.02
				26 ± 1	0.03 ± 0.005

^aThe rod or branch length, *L*, the rod diameter, *d*, and the branch diameter, *B*, are defined in Figure S3 (SI). The theoretical predictions of the tumbling diffusion coefficients, Θ_{TG} , are made according to the hydrodynamic theory of ellipsoids,⁴⁴ eq 4. DLS data: \mathcal{R} is the depolarization ratio (eq 2), taken as a measure of the average anisotropy; $R_{\text{h,T}}$ and $R_{\text{h,R}}$ are the hydrodynamic radii (eq 3). The ratio $(L/B)_{\text{TEM}}$ is the average value measured from TEM images.²³ FCS data: Θ_{TG} computed⁴⁴ for the CTAB and the CTAB+PEG samples from the L_{TEM} and d_{TEM} values (first two rows). For the LSB samples we have computed effective radii according to the Stokes–Einstein relations for a spherical nanoparticle. The stock concentrations (conc) are computed from the extrapolation of the ACF to zero lag times. All data are reported at the temperature of $T = 20$ °C. ^bIndicates that the GNRs or GNSs have been pegylated with PEG₂₀₀₀SH.

employing eq 4, that accounts for hydrodynamic friction for cylinders,⁴⁴ and by assuming the values of the length and the axial ratio of the GNRs measured by TEM (L_{TEM} and $(L/d)_{\text{TEM}}$). These values, reported as Θ_{TG} in Table 1, are in excellent agreement with the measured rotational diffusion coefficients for the different batches of GNRs. The translational diffusion coefficient, $D = 8.5 \pm 0.8 \mu\text{m}^2/\text{s}$, of the unpegylated GNRs ([CTAB] = 0.2 M) is also in good agreement with the prediction of eq 4, $D \cong 13 \mu\text{m}^2/\text{s}$. The lower value measured for the GNRs treated with PEG₂₀₀₀SH, $D = 4.3 \pm 0.2 \mu\text{m}^2/\text{s}$, is probably due to the presence in the suspensions of spherically symmetric objects that are therefore not contributing to the rotational component of g_{VV} . The prepared GNRs appear then to retain the cylindrical shape in aqueous suspension with limited extent of aggregation.

For GNSs we find very similar values for the translational, $R_{\text{h,T}}$, and rotational, $R_{\text{h,R}}$, hydrodynamic radii (eq 3), in agreement with their less elongated structure. The values of $R_{\text{h,T}}$ and $R_{\text{h,R}}$, very close to 23 nm, do not show a marked dependence on the LSB concentration (Table 1). However, the depolarization ratio (\mathcal{R} in eq 2) and therefore the overall shape anisotropy,²³ does increase with the LSB concentration (Table 1, Figure S3, SI). The light-scattering data indicate therefore that the GNSs retain a reduced overall shape anisotropy in suspensions with respect to the GNRs. This result is in agreement with the branched structures observed by TEM imaging (Figure S2, SI). The average encumbrance of the pegylated GNSs (Table 1) is similar to that found for the unpegylated GNSs, indicating that GNSs are not undergoing dramatic aggregation upon pegylation.

Similarly to the gold nanorods,^{27,28} the branched nanostar structures display remarkable luminescence probably induced by the sequential absorption of two photons in the NIR region of the spectrum.⁵⁷ The luminescence intensity I_{TPL} from GNRs or GNSs spread on glass cover slides depends on the average excitation power, P_{exc} , as $I_{\text{TPL}} \propto P_{\text{exc}}^\epsilon$ with $\epsilon = 2.1 \pm 0.2$ (GNRs for $0.2 \leq P_{\text{exc}} \leq 0.8 \text{ mW}$) and $\epsilon = 1.95 \pm 0.04$ (GNSs for $0.2 \leq$

$P_{\text{exc}} \leq 1 \text{ mW}$) (Figure 1D). The two-photon nature of the excitation process was further confirmed by the observation that continuous wave (CW) excitation primes negligible TPL from the samples (Figure 2A,B).

The emission TPL spectrum of GNRs and GNSs in aqueous suspension is a broad band in the visible region of spectrum (Figure 2C, D), that arises from recombinations at the L and X edges and that occur for bulk gold at 518 and 654 nm.^{58,59,28} The shape of the TPL spectra is not much dependent on the excitation energy and the LSB concentration (SI, Figure S4). The excitation TPL spectra display a smooth increase for the GNSs (Figure 2E) and a wide peak at about 800 nm for the GNRs (Figure 2F) and in both cases overlap well with the longitudinal plasmon band, indicating that the TPL intensity is governed by the local field enhancement from the plasmon resonance.²⁸

The polarized TPL signal of the GNRs and GNSs can be used as an indicator of their shape anisotropy. A drop of nano-objects suspensions synthesized with [LSB] = 0.35 M, [LSB] = 0.4 M, and [CTAB] = 0.2 M, was dispersed and immobilized onto glass coverslips such that isolated particles could be irradiated by fs-pulsed excitation at their longitudinal plasmon resonance wavelength ($\langle P \rangle = 0.2 \text{ mW}$ on the sample). The single particle signal changed as a function of the laser polarization angle, θ , and it was fit to the trial function: $I_{\text{TPL}} = I_{\text{TPL,min}} + (I_{\text{TPL,mix}} - I_{\text{TPL,min}})\cos^4(\theta)$, (Figure 3A,B).²⁷ The TPL polarization was computed according from the best fit parameters as:

$$\nu = \frac{I_{\text{TPL,max}} - I_{\text{TPL,min}}}{I_{\text{TPL,max}} + I_{\text{TPL,min}}} \quad (8)$$

For GNRs the polarization ν is close to 1 (Figure 3C) with approximately 60% of probability to have $\nu > 0.9$, $P_{\nu \geq 0.9} \cong 60 \pm 12\%$. Also for GNSs the polarization reaches high levels, $\nu \cong 0.7 - 0.9$, and increases slightly with the LSB concentration and the GNS aspect ratio (Figure 3D). However, the average shape

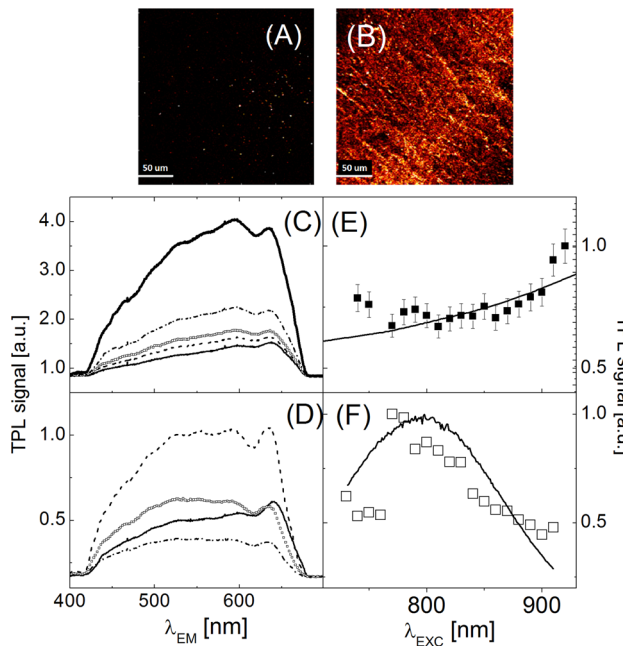


Figure 2. (A) TPL images of the gold nanorods spread on a glass slide under CW laser irradiation at $\lambda_{\text{exc}} = 800 \text{ nm}$. (B) TPL images of the gold nanostars spread on a glass slide under pulsed laser irradiation (80 MHz repetition rate –100 fs laser pulses, $\lambda_{\text{exc}} = 800 \text{ nm}$). (C) Emission spectra of gold nanostars ($[\text{LSB}] = 0.45 \text{ M}$; $\lambda_{\text{exc}} = 750 \text{ nm}$ (solid line); $\lambda_{\text{exc}} = 800 \text{ nm}$ (dash line); $\lambda_{\text{exc}} = 850 \text{ nm}$ (open square line); $\lambda_{\text{exc}} = 900 \text{ nm}$ (dot-dot-dash line); $\lambda_{\text{exc}} = 920 \text{ nm}$ (thick solid line)). (D) Emission spectra of GNRs ($[\text{CTAB}] = 0.2 \text{ M}$; $\lambda_{\text{exc}} = 750 \text{ nm}$ (solid line); $\lambda_{\text{exc}} = 800 \text{ nm}$ (dash line); $\lambda_{\text{exc}} = 850 \text{ nm}$ (open squares); $\lambda_{\text{exc}} = 900 \text{ nm}$ (dot-dot-dash line)). (E,F) TPL excitation spectra, corrected for the setup transmission, of the gold nanostars (E) and gold nanorods (F). The corresponding one photon extinction spectra are reported on the same panels as a solid line.

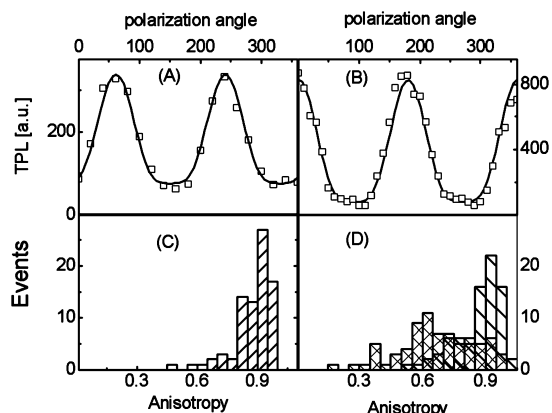


Figure 3. (Top) Dependence of TPL emission on incident polarization for GNRs synthesized from $[\text{LSB}] = 0.3 \text{ M}$ (A) or from $[\text{CTAB}] = 0.2 \text{ M}$ seed growth (B). The fit to a $\cos(\theta)^4$ trend are reported as continuous lines. (Bottom) Histograms of the anisotropy distribution for the GNRs obtained from 0.2 M CTAB seed growth (C) and for the GNSs obtained from $[\text{LSB}] = 0.3 \text{ M}$ (cross-hatched bars) and $[\text{LSB}] = 0.4 \text{ M}$ (slanted bars) seed growth (D).

anisotropy of the GNSs, as it can be measured from the probability $P_{\nu \geq 0.9}$, is much lower than that of the GNRs, since $P_{\nu \geq 0.9} ([\text{LSB}] = 0.3 \text{ M}) = 12 \pm 4\%$ and $P_{\nu \geq 0.9} ([\text{LSB}] = 0.4 \text{ M}) = 40 \pm 9\%$, compared to $P_{\nu \geq 0.9} ([\text{CTAB}] = 0.2 \text{ M}) \cong 60 \pm 12\%$.

Therefore, the polarization studies confirm that the GNSs have reduced values of the overall shape anisotropy.

For cell imaging applications and treatment with GNRs and GNSs we need to know their TPL brightness and number concentration. These values were derived from the analysis of the fluorescence ACFs collected on diluted (1:5–1:20) suspensions of the GNRs and GNSs. The translational and rotational diffusion components could be easily separated in the fluorescence ACFs (eq 5) since they fall in the millisecond (translational) and microsecond (rotational) time regime. As for the case of the dynamic light-scattering measurements we have analyzed the diffusion coefficients in terms of hydrodynamic modeling of the nanoparticle diffusion (eq 4), finding good agreement with the prediction that can be made on the basis of the structural parameters obtained by TEM (Table 1).

The number concentration of the stocks suspensions of the GNRs and GNSs was derived from the zero lag time extrapolation of the correlation function (eq 5), $g(0)$, and corrected for the dilution used in FCS experiments (Table 1). The NP volume was computed from the TEM structural data (for the GNRs), or by assuming an effective spherical volume, $V_{\text{eff}} = 4\pi R_{\text{hR}}^3/3$ (for the GNSs). In doing so we could estimate the mass concentration for the GNRs ($C \cong 0.05 \text{ mg/mL}$) and for the GNSs ($C \cong 0.05\text{--}0.03 \text{ mg/mL}$) stock suspensions. These values are in good agreement with the gold concentrations measured by ICP-OES, 0.03–0.07 mg Au/mL (see SI for details).

The TPL brightness of the GNRs and GNSs in aqueous solutions was evaluated from the analysis of the photon counting histogram in terms of the PCH model developed by Gratton et al.⁶⁰ These measurements were performed at $P_{\text{exc}} \cong 16 \text{ mW}$, since at this value no detectable autofluorescence signal from the cells was observed (see below). The results, summarized in Table 2, indicates an average brightness for the GNSs that is about 7–10 times larger than that of rhodamine 6G in ethanol.

Table 2. Brightness Values for the NPs in Suspensions in Which the Growth Was Obtained by LSB or CTAB^a

growth seed concentration [M]	brightness [kHz/nanopart.]
LSB	210 ± 20
0.6	130 ± 30
0.45	130 ± 40
0.2	110 ± 40
CTAB	
0.2	15 ± 3
Rh6G(ethanol)	

^aThe values are computed from the analysis of the photon counting histograms. For all measurements, $P_{\text{exc}} = 16 \text{ mW}$. The excitation wavelength was $\lambda_{\text{exc}} = 800 \text{ nm}$.

Having estimated the concentration of the GNRs and the GNSs, we could identify the optimal conditions for potential application to *in vivo* cell imaging. For these experiments the stock suspensions were further 10 times concentrated in order not to dilute excessively the cell culture medium with surfactants. We studied the cytotoxic effect of GNRs ($[\text{CTAB}] = 0.2 \text{ M}$ growth seed solution) and GNSs ($[\text{LSB}] = 0.35 \text{ M}$ growth seed solution) on three cell lines, the HeLa, the A549 and the HEK293 cells. The cell viability was tested after treatment for 4 and 24 h under increasing concentrations

($1.25 \leq C \leq 100 \mu\text{g/mL}$) of the nano-objects. The data summarized in Figure 4 indicate that the percentage of cells in

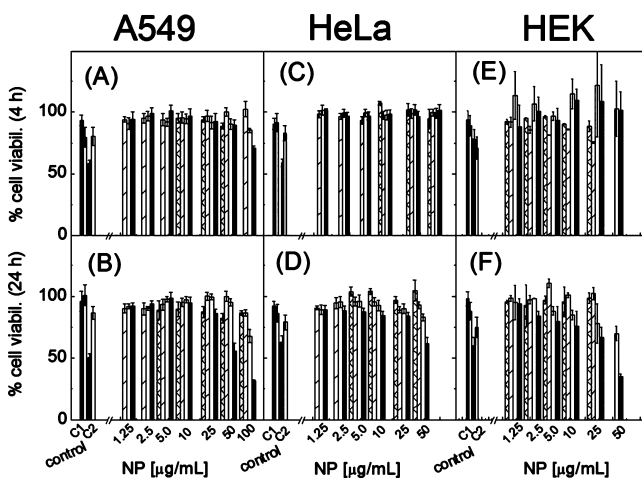


Figure 4. Cell viability as a function of increasing concentration of GNRs and GNSs (in $\mu\text{g/mL}$ of gold). Left column: viability of A549 cells at 4 h (A) and at 24 h (B). Middle column: viability of the HeLa cells at 4 h (C) and at 24 h (D). Right column: viability of the HEK293 cells at 4 h (E) and at 24 h (F). The GNRs and GNSs were prepared from $[\text{CTAB}] = 0.2 \text{ M}$ growth seed solutions and $[\text{LSB}] = 0.35 \text{ M}$ growth seed solutions. The data refer to the GNRs (filled bars), the GNSs (open bars), and the pegylated form of the GNRs (cross-hatched bars) and GNSs (slanted bars). The control data refer to the viability of the two cell lines after treatment with the surfactants alone at the highest (C2) and the lowest (C1) concentrations: filled and open bars refer to CTAB and LSB, respectively.

viable conditions decreases only slightly (viability $\geq 72\text{--}96\%$) with the concentration of the GNSs up to about $50 \mu\text{g/mL}$ even after a prolonged treatment ($\geq 24 \text{ h}$). On the contrary the GNRs display a clear toxic effect ($\geq 30\text{--}60\%$ cell viability) on all the cell lines at $C = 50 \mu\text{g/mL}$ after 24 h treatment. For this reason we tested also the pegylated form of the GNRs and the GNSs treated with $\text{PEG}_{2000}\text{SH}$, that gave indeed reduced toxicity (Figure 4, cross-hatched and slanted bars), in agreement with the literature.^{12,61} Among the cell lines, the HeLa cells appear to be more stable than the HEK and A549 cell lines at concentrations of nano-objects $\geq 10\text{--}15 \mu\text{g/mL}$.

The toxicity observed here is also partially due to the direct effect of the surfactants on the cells. In fact, the treatment of the cells with the surfactants alone, at the same dilution as that used for the cell treatment with the GNRs or GNSs, had a clear effect on the cell viability particularly for the CTAB surfactant at the highest concentration (Figure 4, control, C2). The particles grown with the less toxic LSB surfactant should then provide an intrinsically reduced cytotoxic effect.

Regarding the direct role of the nanoparticles on the cell toxicity, we should consider that the negatively charged gold nanostars is expected to be internalized via endocytotic routes (see also hereafter), with reduced toxicity. Small (size $\leq 20 \text{ nm}$), positively charged nanoparticles have been reported to be internalized via pore formation in supported bilayers. Possible perturbation of the delicate concentration balance of intra-cellular vs extracellular ions could then occur in cells for cationic nanoparticles.^{25,38}

We evaluated the overall cellular uptake by measuring the average TPL signal of the GNRs and GNSs in cells. The nanoparticles in pegylated and unpegylated form were used at 7

$\mu\text{g/mL}$ to treat tissue plated A549, HeLa, and HEK293 cells. TPL images of untreated cells were compared to those of cells treated for 1 or 4 h at $T = 4^\circ\text{C}$ or $T = 37^\circ\text{C}$ before imaging (Figure 5). The position of the cells was identified by their

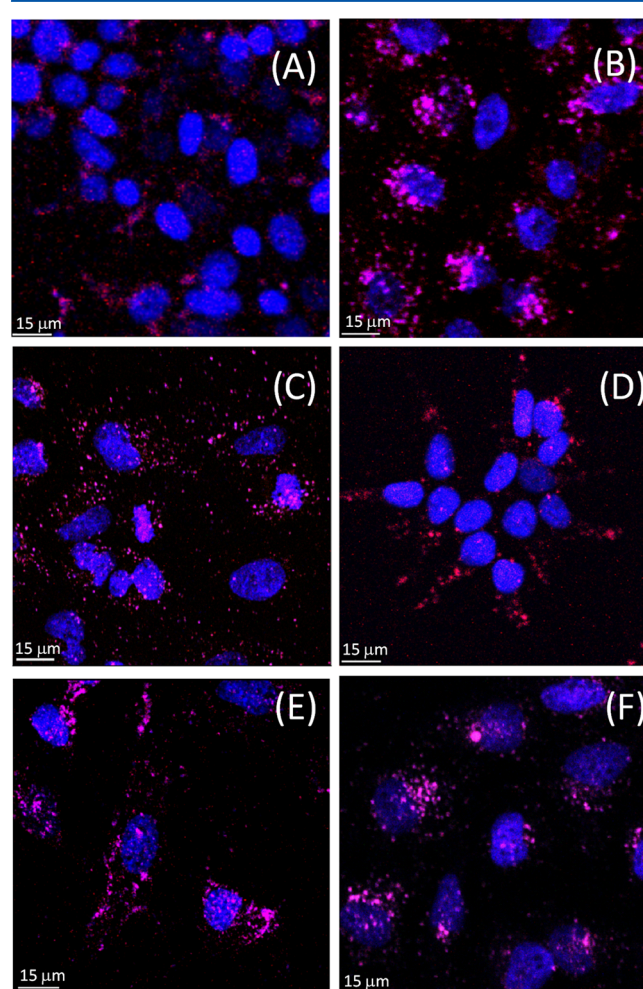


Figure 5. Cellular uptake of the NPs monitored from the red TPL emission (emission filter 600/40) of the GNRs and GNSs. Excitation wavelength and power were $\lambda_{\text{exc}} = 800 \text{ nm}$ and $P_{\text{exc}} \geq 16 \text{ mW}$. The cell nuclei were stained by DAPI (blue channel; emission filter 485/30). Experiments were performed on the A549 cells (A and B), on the HEK cells (C and D) and on the HeLa cells (E and F). All cells were treated for 4 h at 37°C with $C = 7 \mu\text{g/mL}$ suspensions of nonpegylated gold nanostars ($[\text{LSB}] = 0.35 \text{ M}$, [A, C, E]) or nanorods ($[\text{CTAB}] = 0.2 \text{ M}$, [B, D, F]). All the images (512×512) are the result of 5 kalman average scans with $10 \mu\text{s}$ of residence time per pixel. The white bar represents the $15 \mu\text{m}$ size.

DAPI stained nuclei, the autofluorescence emission was mainly detected in the green channel (535/50 band-pass filter) and the red emission (600/40 band-pass filter) was used to monitor the presence of the GNRs and GNSs. No substantial bleeding of autofluorescence into the red channel or bleaching were detected for excitation powers lower than $\geq 16 \text{ mW}$ (SI, Figure S5). We can then visualize (Figure 5) the internalization of the GNRs and GNSs by HeLa, A549, and HEK293 cells by superimposing the blue (nuclei) and the red (GNRs or GNSs) channels. Both the GNSs and the GNRs localize mostly in lumps (Figure 5) though a diffuse fainter red signal is present also in the cells. Similar images have been reported also in the case of cell specific targeting.^{62,63}

We quantified then the overall internalization efficiency of the GNSs and the GNRs by computing the red channel content averaged over nuclei centered ROIs whose radius was $\geq 30\%$ larger than that of the corresponding cell nucleus. This method was applied to different treatment conditions, different cell lines, and two batches of nanoparticles. Regarding the cell lines, the HeLa cells seem to internalize more efficiently than the A549 and HEK293 cells (Figure 6). The largest luminescence

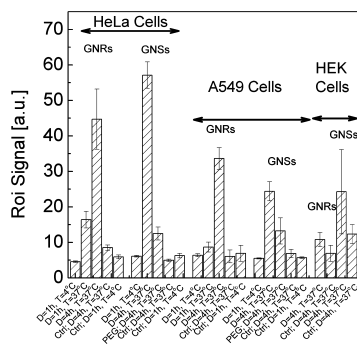


Figure 6. Cellular uptake of the NPs monitored from the red TPL emission (emission filter 600/40) of the gold nanostars and gold nanorods. The plot reports the average red emission measured on nucleus-centered ROIs encompassing an area 70% larger than the cell nucleus. The x-axis indicates the duration (D) in hours and the temperature of the incubation. The control images taken on untreated cell lines (A549 Ctrl and HeLa Ctrl) are reported on the side of the plot. The bar on the images corresponds to $50 \mu\text{m}$.

signal was found for the gold nanostars in the HeLa and HEK cells, whereas the trend was somehow reversed in the A549 cell line. These differences are, however, affected by systematic uncertainties due to the number of cells (the cells were grown to confluence) and the slight difference in the TPL brightness (Table 2). Very similar internalization efficiencies of the two kinds of nanoparticles were, in fact, detected by ICP optical spectrometry experiments (see SI, Table S2) on treated HEK cells.

Pegylation, as expected, considerably reduced the nanoparticle uptake, particularly by tumor HeLa cells. Finally, we observed that at 4°C of incubation temperature the internalization was almost suppressed both for the gold nanorods and for the gold nanostars (Figure 6). Due to this latter dependence, it is likely that the nanoparticles investigated here are taken up by cells by a nonspecific process of endocytosis and concentrate in endosomes²⁵ that might then be the luminescent nano-objects detected in the cells (Figures 5 and 7A). We will refer for the sake of simplicity to “endosome” in the following to indicate the luminescent nanoparticle including organelles observed in the cells.

The degree of internalization and toxicity of the nanoparticles may depend on their surface properties.²⁵ The role of the surface charge has been brought into evidence also in the present study by comparing nanoparticles grown in the LSB (zwitterionic) and CTAB (cationic) surfactants. However, the overall shape and size have also been reported to have an effect on the internalization efficiency.³⁷ Since the suspension of the nanoparticles in the cell growth buffers may induce their aggregation, it seems relevant to ascertain the effective size of the gold nanostars that interact with the cells. The next step is to have information on the state of the nanoparticles within the cells (aggregation number within the endosomes), and to this

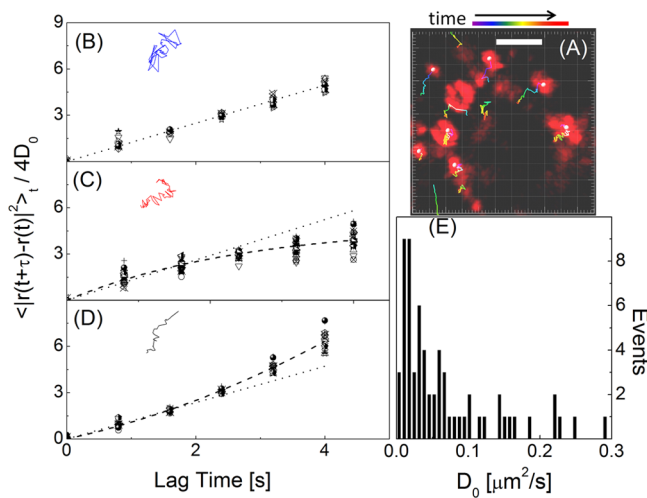


Figure 7. Tracking of single luminescent nano-objects in cells (red channel, emission filter 600/40). (A) Snapshot of the image sequence (50 s total duration) with the tracks of the segmented objects. The time is color coded in the tracks (rainbow bar). The white bar represents the size of $5 \mu\text{m}$ on the image. (B–D) Examples of the mean square displacement normalized to the initial slope, $\Delta^2(\tau) = \langle |r(t + \tau) - r(t)|^2 \rangle / 4D_0$. The solid segmented curves in these panels represent typical tracks of the subset reported in each panel. (B, C, D) Correspond respectively to the pure diffusive, subdiffusive (constrained diffusion), and superdiffusive (drift motion) cases. The dashed and the solid lines in each panel represent the pure diffusive motion and the constrained diffusion (C), or the drift motion (D) $\Delta^2(\tau) = 2D\tau + V^2\tau^2$. (E) Distribution of the diffusion coefficients as derived from the initial slope of the mean square displacement, D_0 .

purpose we studied the motion of the endosomes by combining direct tracking and fluorescence correlation methods.

By performing time-lapse acquisitions of cells treated with gold nanostars (emission filter 600/40; TPL emission of the nanoparticles), several internalized objects (Figure 7A and movies in the SI) could be followed in their motion within the cells. About 80 trajectories (Figure 7) were reconstructed and characterized by computing the mean square displacement $\Delta^2(\tau) = \langle |r(t + \tau) - r(t)|^2 \rangle_t$ as a function of time (Figure 7B–D). By following different endosomes within the cells, three kinds of behavior can be found for $\Delta^2(\tau)$ that can be analyzed in terms of linear, sublinear, or superlinear trends. In order to compare the analysis of the different tracked objects we normalized their mean square displacement to the initial slope D_0 of $\Delta^2(\tau)$, as obtained from the linear fit of $\Delta^2(\tau)$ on the three shortest lag times. The linear trend of $\Delta^2(\tau)$ (Figure 7B) is ascribed to a diffusive motion in two dimensions ($\Delta^2(\tau) = 4D\tau$). The sublinear and superlinear trends (Figure 7C and D) can be ascribed to constrained diffusion⁶⁴ and to drift motion, respectively.⁶³ These two latter cases are likely due to the active motion of endosomes engulfed with nanoparticles along the microtubules.^{63,65} This analysis is also supported by the visual inspection of the tracks, such as those reported for example in Figure 7B–D. As can also be verified from the movies reported in the SI, the motion of the particles within the cell comprise a slow drift motion on which distinct time stretches of constrained diffusion are superimposed (see for example the track reported in Figure 7C). The average diffusion coefficient of the endosomes within the cell is $D_0 = 0.07 \pm 0.05 \mu\text{m}^2/\text{s}$. On the other hand the upward curvature observed in Figure 7D is compatible with drift motion and can be fit to $\Delta^2(\tau) = 2D\tau + V^2\tau^2$.

$V^2\tau^2$.¹³ In this way we estimate an average drift speed, $V = 0.1 \pm 0.05 \mu\text{m/s}$.

Tracking can provide us with a detailed picture of the intracellular motion, but it cannot be applied to extracellular medium where the characteristic motion times of the nanoparticles are much shorter. A detailed picture of both situations can be gained by focusing on a single spot (in and/or out of the cell) and by performing correlation spectroscopy. In this case we miss the wide field description of the motion, but we reach the time resolution to follow the fluorescence fluctuations both inside and outside HEK293 cells treated with GNRs and GNSs (treatment time ≤ 1 h). The fluorescence signals collected within the cells were acquired 1.2 μm above the detected Petri dish coverslip. The beam waist, evaluated from a Gaussian fit of the beam profile on the CCD plane, is $\omega_0 \cong 0.6 \mu\text{m}$ and corresponds to a Rayleigh range⁶⁶ $z_R \cong 1.4 \mu\text{m}$. Since the HEK293 cell thickness is $\cong 6 \mu\text{m}$,⁶⁷ the traces acquired within the cells are only partially affected by the fluorescence fluctuations arising from NPs on the cell membrane or diffusing above it.

The fluorescence traces always contain sharp peaks (Figure 8A, B). However, those traces acquired within the cells are characterized by a much wider frequency spectrum than the extracellular traces. We ascribe the fluorescence bursts (typically 10–100 s of ms wide) to the diffusion of the endosomes through the excitation volume. The slow ($\cong 10$ s) fluorescence fluctuations in the intracellular traces may be due to the movement of the cell membranes out of the laser focus and to the drift motion (see Figure 7D) of the endosomes through the beam waist. This picture is supported by the analysis of the movements of the membranes of untreated cells, observed by transmission wide field imaging, which typically occur on the 5–10 s time scale (see SI, Figure S7) and by the direct observation of the traces of the luminescent nano-objects diffusing in the cells (Figure 7). From the value $D_0 = 0.07 \pm 0.05 \mu\text{m}^2/\text{s}$ and $V = 0.1 \pm 0.05 \mu\text{m/s}$, derived from the mean square displacement analysis, we estimate the diffusion and drift times^{52,53} as follows: $\tau_D = \omega_0^2/8D \cong 560 \text{ ms}$ and $\tau_{\text{drift}} = \omega_0/V \cong 6 \text{ s}$. The drift motion of the endosomes and the membrane movements occur then on the same time scale, and the two motions cannot be sorted out in the correlation function decay. Therefore, we focus on the diffusive components of the intracellular motion by filtering out the components slower than 10 s in the ACF,⁶⁸ as described in the SI (Figure S6 and eq S1). This algorithm will also partially reduce the influence of the drift motion on the fluorescence correlation functions.

The fluorescence fluctuations ACFs have two very distinct behaviors when computed inside or outside the cells. The diffusion times of the unpegylated GNRs and GNSs in the cell culture medium (at $T = 37^\circ\text{C}$, Figure 8C) are $\tau_D = 25 \pm 4 \text{ ms}$ and $\tau_D = 4.5 \pm 0.8 \text{ ms}$, respectively, and no anomalous diffusion or drift motion can be brought into evidence ($\alpha \cong 1 \pm 0.1$ and $\tau_V > 20 \text{ s}$ in eq 7). The corresponding values of the hydrodynamic radii, $R_h = 110 \pm 12 \text{ nm}$ (GNRs) and $R_h = 58 \pm 5 \text{ nm}$ (GNSs), indicate that both types of unpegylated nanoparticles are undergoing some aggregation when dispersed in cell culture media (see Table 1). If we assume a fractal aggregation for the nano-objects,^{69,70} we can estimate the aggregation number $N_{\text{agg}} \cong (R_h/R_T^{\text{eff}})^{2.2} \cong 10$ and 3 for the GNRs and the GNSs samples, respectively.

The ACFs of the fluorescence fluctuations arising from GNSs within the cells cannot be satisfactorily fit to the pure Brownian diffusion model (eq 7 with $\alpha = 1$, $\tau_V > 30 \text{ s}$; black solid line in

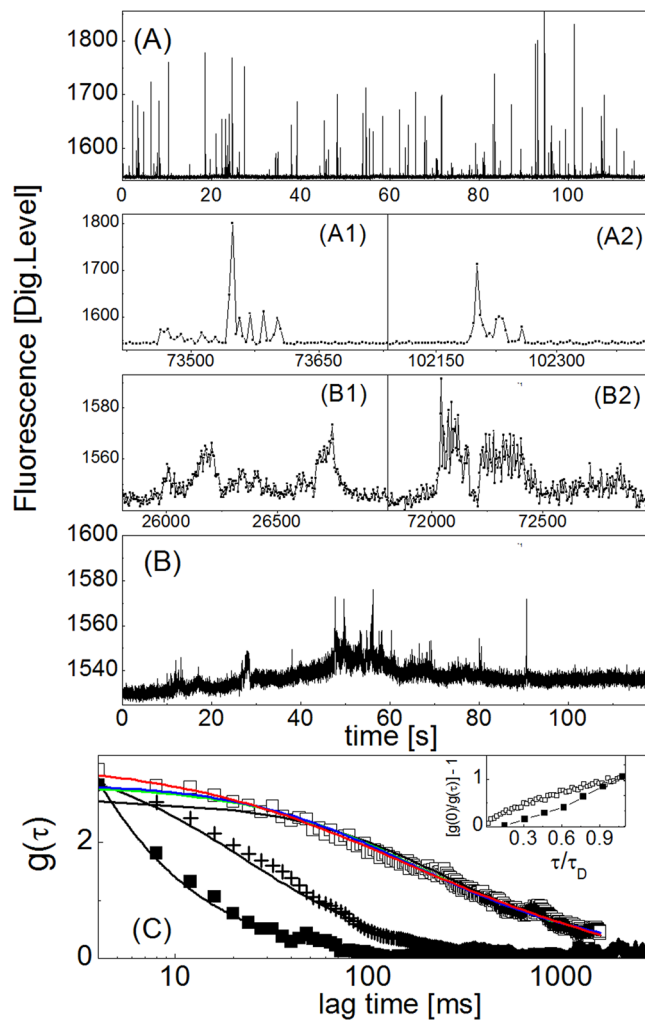


Figure 8. Examples of fluorescence traces collected on spots outside (A) and inside (B) the cell cytoplasm. All data were measured at $T = 37^\circ\text{C}$. (A1, A2) Blow-ups of the trace in panel A. (B1, B2) Blow-ups of the trace in panel B. (C) Correlation functions of the TPL trace collected from GNRs (crosses) in the cell culture medium and from the GNSs in the cell culture medium (■) and in the cell cytoplasm (□). The correlation functions reported here are averages over 100 windows of 20 s duration time each (see eq S1 in SI). The solid lines are the best fit of the data to eq 7. For the extracellular data (solid lines) we set $\alpha = 1$ and $\tau_V > 30 \text{ s}$ finding $\tau_D = 25 \pm 4 \text{ ms}$ and $\tau_D = 4.5 \pm 0.8 \text{ ms}$ for the gold nanorods and nanostars, respectively. For the ACF of the intracellular data we obtained: $\alpha = 1$ and $\tau_V > 30 \text{ s}$ (black line); $\alpha = 1$, $\tau_V = 1.6 \pm 0.5 \text{ s}$ (green line); $\alpha = 0.7 \pm 0.1$, $\tau_V > 30 \text{ s}$ (blue line); $\alpha = 0.72 \pm 0.07$, $\tau_V = 3.4 \pm 0.25 \text{ s}$ (red line). The inset of panel C reports the inverse of the correlation function, $g^{-1}(\tau)|_{\tau=0} \approx g^{-1}(0)(1 + (\tau/(\tau_D))^\alpha)$, as a function of time for the gold nanostar data.

Figure 8C). The ACFs cannot be adequately described by either the addition of a drift component in the function decay (eq 7 with $\alpha = 1$, $\tau_V = 1.6 \pm 0.5 \text{ s}$; green line in Figure 8C) or the assumption of a pure anomalous diffusion without any drift motion component in the ACF (eq 7 with $\alpha = 0.7 \pm 0.1$, $\tau_V > 30 \text{ s}$; blue line in Figure 8C). An excellent description of the intracellular ACF over almost three decades of lag times can be obtained instead by assuming anomalous diffusion superimposed with a drift motion (eq 7 with $\alpha = 0.72 \pm 0.07$, $\tau_V = 3.4 \pm 0.25 \text{ s}$; red line in Figure 8C). The best fit diffusion time obtained with such a model is $\tau_D = 145 \pm 35 \text{ ms}$ almost 30 times larger than the free diffusion in the extracellular medium.

The presence of anomalous diffusion can be gained from the downward curvature of the function $g^{-1}(\tau)|_{\tau \approx 0} \approx g^{-1}(0)(1 + (\tau/(\tau_D)^\alpha))$ for small lag times (inset in Figure 8C). It is noteworthy that the presence of both the anomalous diffusion (Figure 7C) and the drift component (Figure 7D) in the intracellular motion of the luminescent endosomes has been directly observed on the microscopic movies and confirmed by the autocorrelation methods. The diffusion times evaluated with the two methods differ ($\cong 4$ times) probably because of the high pass filtering of the traces for the ACF computation and the wide D_0 distribution observed in Figure 7E.

No direct estimate of the nanoparticle loading of the endosomes can be drawn from their intracellular diffusion time since the intracellular viscosity is affected by a large variability.⁷¹ However, we can measure the overall amount of gold internalized by the HEK cells (see SI “ICP optical spectrometry of treated cells”) and correlate it with the average number of nano-objects observed in the cells.

For the HEK cells treated with gold nanostars and gold nanorods we measured an average of 1360 ± 80 nanostars and 1750 ± 180 nanorods per cell. The efficiency of internalization can be evaluated as the ratio of the internalized gold (in μg) to the total amount of gold used for the cell treatments, reported to the case of 10^6 treated cells. This quantity (estimated in Table S2 in SI, % Au_{cell}) is very similar for the cases of nanostars ($19 \pm 1\%$) and nanorods ($24 \pm 3\%$), therefore confirming that the two types of nanoparticles are very similarly internalized by the cells. We can qualitatively estimate the number of the endosomes, $\cong 15-20$, on a single 2D section of the cells (Figures 5 and 7). This estimate can be refined by analyzing the frequency of the luminescence bursts observed in traces such as those reported in Figure 8B. The intracellular luminescence traces, filtered for the slowly relaxing dynamics (cutoff frequency 1.25 s^{-1} , Figure S8 [SI]), show that the bursts appear bunched in sparse events whose average frequency is $\gamma_R^{(\text{in})} = 0.07 \pm 0.02 \text{ Hz}$. These events correspond to the drift motion observed in the stop-and-go trajectories of a population of tracked endosomes (see Figure 7C). The occurrence frequency of the burst bunches in the traces of Figure 8B is related to the number concentration, n , and the drift velocity, V , (see eq S5 in SI) as⁷² $\gamma_R^{(\text{in})} \cong 4\pi((nw_0^3)/(\tau_V))$. From the value of $\tau_V \cong 3\text{s}$, measured from the mean square displacement of the luminescent endosomes, and $\gamma_R^{(\text{in})} = 0.07 \pm 0.02 \text{ Hz}$ we estimate $n \cong 0.07 \pm 0.02 \text{ organelles per } \mu\text{m}^3$ that corresponds to about 40 organelles per cell ($5 \mu\text{m}$ in radius). These figures, together with the measure of the total amount of gold internalized per cell, indicate that an average of 35–45 nanoparticles are internalized per observed luminescent endosome in the cells.

In summary the GNSs developed by LSB-mediated seed growth are internalized in a way similar to that of the GNRs by various cell lines and display cellular toxicity lower than that of GNRs, taken here as a reference of anisotropic NPs. Pegylation of the GNSs depresses their internalization and increases their resistance to aggregation in the culture medium. The good internalization efficiency may be ascribed to the overall spherical shape of the GNSs, as detected by various solution techniques. The high axial ratio of their branches on the other hand, ensures that GNSs retain a strong two-photon luminescence, similar to that displayed by high aspect ratio GNRs. By exploiting the good TPL signal of the nanoparticles we have followed the nanoparticle including organelles in their motion in the cells that appear to be a superposition of a drift

motion, probably along the microtubules,⁶³ and of a confined diffusive movement.

The direct estimate of the concentration of intracellular diffusing nano-objects does not imply a direct interaction of the NPs with the cytoplasm, since the GNSs are probably internalized by endocytosis. To this purpose one should impart to the GNSs additional properties to obtain the disruption of endosomes or the internalization through “sponge-effect” mechanisms⁷³ or conjugation with natural cell-penetrating-/fusogenic chaperones.⁷⁴ For cancer therapy, specific targeting could instead be obtained by conjugation of the GNSs with nanobodies.⁶² Future developments of imaging and photothermal applications of the poorly exploited GNSs can be envisioned on the basis of the present results.

ASSOCIATED CONTENT

S Supporting Information

Additional experimental details and movies of time-lapse acquisitions of cells treated with gold nanostars where endosomes were followed in their motion within the cells. This material is available free of charge via the Internet at <http://pubs.acs.org>.

AUTHOR INFORMATION

Corresponding Author

*E-mail: psp@unipv.it (P.P.). E-mail: giuseppe.chirico@mib.infn.it (G.C.).

Notes

The authors declare no competing financial interest.

ACKNOWLEDGMENTS

The research described herein has been partially supported by a grant of the Fondazione Cariplo to P.P. and G.C. (Bandi Ricerca Scientifica e Tecnologica sui Materiali Avanzati no. 2010-0454) and by Regione Lombardia (Project SAL-45). We gratefully thank Dr. Lucia Cucca (university of Pavia) for the ICP optical and mass spectrometry measurements and Dr. Ivan Zanoni and Prof. F. Granucci for cell cultures.

REFERENCES

- Huang, X.; Prashant, K. J.; El-Sayed, I. H.; El-Sayed, M. A. Plasmonic photothermal therapy (PPTT) using gold nanoparticles. *Lasers Med. Sci.* **2008**, *23*, 217–228.
- Huang, X.; Jain, P. K.; El-Sayed, I. H.; El-Sayed, M. A. Gold nanoparticles: Interesting optical properties and recent applications in cancer diagnostics and therapy. *Nanomedicine* **2007**, *2*, 681–693.
- Huang, H.-C.; Barua, S.; Sharma, G.; Dey, S. K.; Rege, K. Inorganic nanoparticles for cancer imaging and therapy. *J. Controlled Release* **2011**, *155*, 344–357.
- Durr, N. J.; Larson, T.; Smith, D. K.; Korgel, B. A.; Sokolov, K.; Ben-Yakar, A. Two-photon luminescence imaging of cancer cells using molecularly targeted gold nanorods. *Nano Lett.* **2007**, *7*, 941–945.
- Sokolov, K.; Follen, M.; Aaron, J.; Pavlova, I.; Malpica, A.; Lotan, R.; Richards-Kortum, R. Real-time vital optical imaging of precancer using anti-epidermal growth factor receptor antibodies conjugated to gold nanoparticles. *Cancer Res.* **2003**, *63*, 1999–2004.
- Murphy, C. J.; Gole, A. M.; Hunyadi, S. E.; Stone, J. W.; Sisco, P. N.; Alkilany, A.; Kinard, B. E.; Hankins, P. Chemical sensing and imaging with metallic nanorods. *Chem. Commun.* **2008**, 544–557.
- Perez-Juste, J.; Pastoriza-Santos, I.; Liz-Marzan, L. M.; Mulvaney, P. Gold nanorods: Synthesis, characterization and applications. *Coord. Chem. Rev.* **2005**, *249*, 1870–1901.

- (8) Sonnichsen, C.; Alivisatos, A. P. Gold nanorods as novel non-bleaching plasmon-based orientation sensors for polarized single-particle microscopy. *Nano Lett.* **2005**, *5*, 301–304.
- (9) Nel, A. E.; Madler, L.; Velegol, D.; Xia, T.; Hoek, E. M. V.; Somasundaran, P.; Klaessig, F.; Castranova, V.; Thompson, M. Understanding bio-physics-chemical interactions at the nano-bio interface. *Nat. Mater.* **2009**, *8*, 543–557.
- (10) Daniel, M.-C.; Astruc, D. Gold nanoparticles: Assembly, supramolecular chemistry, quantum-size-related properties, and applications toward biology, catalysis, and nanotechnology. *Chem. Rev.* **2004**, *104*, 293–346.
- (11) Lakowicz, J. R. Plasmonics in biology and plasmon-controlled fluorescence. *Plasmonics* **2006**, *1*, 5–33.
- (12) Lewinski, N.; Colvin, V.; Drezek, R. Cytotoxicity of nanoparticles. *Small* **2008**, *4*, 26–49.
- (13) Huff, T. B.; Tong, L.; Zhao, Y.; Hansen, M. N.; Cheng, J. X.; Wei, A. Hyperthermic effects of gold nanorods on tumor cells. *Nanomedicine* **2007**, *2*, 125–132.
- (14) Tong, L.; Wei, Q.; Wei, A.; Cheng, J. X. Gold nanorods as contrast agents for biological imaging: optical properties, surface conjugation and photothermal effects. *Photochem. Photobiol.* **2009**, *85*, 21–32.
- (15) Skrabalak, S. E.; Chen, J.; Au, L.; Lu, X. M.; Li, X.; Xia, Y. Gold nanocages for biomedical applications. *Adv. Mater.* **2007**, *19*, 3177–3184.
- (16) Yong, K.-T.; Swihart, M. T.; Ding, H.; Prasad, P. N. Preparation of gold nanoparticles and their applications in anisotropic nanoparticle synthesis and bioimaging. *Plasmonics* **2009**, *4*, 79–93.
- (17) Burda, C.; Chen, X.; Narayanan, R.; El-Sayed, M. A. Chemistry and properties of nanocrystals of different shapes. *Chem. Rev.* **2005**, *105*, 1025–1102.
- (18) Guerrero-Martínez, A.; Barbosa, S.; Pastoriza-Santos, S.; Liz-Marzán, L. M. Nanostars shine bright for you. Colloidal synthesis, properties and applications of branched metallic nanoparticles. *Curr. Opin. Colloid Interface Sci.* **2011**, *16*, 118–127.
- (19) Anker, J. N.; Hall, W. P.; Lyandres, O.; Shah, N. C.; Zhao, J.; Van Duyne, R. P. Biosensing with plasmonic nanosensors. *Nature Mat.* **2008**, *7*, 442–453.
- (20) Mayer, K. M.; Hafner, J. H. Localized surface plasmon resonance sensors. *Chem. Rev.* **2011**, *111*, 3828–3857.
- (21) Loo, C.; Lowery, A.; Halas, N.; West, J.; Drezek, R. Immunotargeted nanoshells for integrated cancer imaging and therapy. *Nano Lett.* **2005**, *5*, 709–711.
- (22) O’Neal, D. P.; Hirsch, L. R.; Halas, N. J.; Payne, J. D.; West, J. L. Photo-thermal tumor ablation in mice using near infrared-absorbing nanoparticles. *Cancer lett.* **2004**, *209*, 171–176.
- (23) Pallavicini, P.; Chirico, G.; Collini, M.; Dacarro, G.; Donà, A.; D’Alfonso, L.; Falqui, A.; Diaz-Fernandez, Y.; Freddi, S.; Garofalo, B.; Genovese, A.; Sironi, L.; Taglietti, A. Synthesis of branched Au nanoparticles with tunable near-infrared LSPR using a zwitterionic surfactant. *Chem. Commun.* **2011**, *47*, 1315–1317.
- (24) Skirtach, A. G.; Karageorgiev, P.; De Geest, B. G.; Pazos-Perez, N.; Braun, D.; Sukhorukov, G. B. Nanorods as wavelength-selective absorption centers in the visible and near-infrared regions of the electromagnetic spectrum. *Adv. Mater.* **2008**, *20*, 506–510.
- (25) Verma, A.; Stellacci, F. Effect of surface properties on nanoparticle-cell interactions. *Small* **2010**, *6*, 12–21.
- (26) Petrova, H.; Hu, M.; Hartland, G. V. Photothermal properties of gold nanoparticles. *Z. Phys. Chem.—Int. J. Res. Phys. Chem. Chem. Phys.* **2007**, *221*, 361–376.
- (27) Wang, H.; Huff, T. B.; Zweifel, D. A.; He, W.; Low, P. S.; Wei, A.; Cheng, J.-X. In vitro and in vivo two-photon luminescence imaging of single gold nanorods. *Proc. Natl. Acad. Sci. U.S.A.* **2005**, *102*, 15752–15756.
- (28) Wang, D. S.; Hsu, F. Y.; Lin, C. W. Surface plasmon effects on two photon luminescence of gold nanorods. *Opt. Expr.* **2009**, *17*, 11350–11359.
- (29) Park, J.; Estrada, A.; Sharp, K.; Sang, K.; Schwartz, J. A.; Smith, D. K.; Coleman, C.; Payne, J. D.; Korgel, B. A.; Dunn, A. K.; Tunnell,
- J. W. Two-photon-induced photoluminescence imaging of tumors using near-infrared excited gold nanoshells. *Opt. Expr.* **2008**, *16*, 1590–1599.
- (30) Tcherniak, A.; Dominguez-Medina, S.; Chang, W.-S.; Swanglap, P.; Slaughter, L. S.; Landes, C. F.; Link, S. One-photon plasmon luminescence and its application to correlation spectroscopy as a probe for rotational and translational dynamics of gold nanorods. *J. Phys. Chem. C* **2011**, *115*, 15938–15949.
- (31) El-Sayed, M. A. Some interesting properties of metals confined in time and nanometer space of different shapes. *Acc. Chem. Res.* **2001**, *34*, 257–264.
- (32) Kelly, K. L.; Coronado, E.; Zhao, L. L.; Schatz, G. C. The optical properties of metal nanoparticles: The influence of size, shape, and dielectric environment. *J. Phys. Chem. B* **2002**, *107*, 668–677.
- (33) Terentyuk, G. S.; Maslyakova, G. N.; Suleymanova, L. V.; Khlebtsov, N. G.; Khlebtsov, B. N.; Akchurin, G. G.; Maksimova, I. L.; Tuchin, V. V. Laser-induced tissue hyperthermia mediated by gold nanoparticles: Toward cancer phototherapy. *J. Biomed. Opt.* **2009**, *14*, 021016.
- (34) Wust, P.; Hildebrandt, B.; Sreenivasa, G.; Rau, B.; Gellermann, J.; Riess, H.; Felix, R.; Schlag, P. M. Hyperthermia in combined treatment of cancer. *Lancet Oncol.* **2002**, *3*, 487–497.
- (35) Link, S.; El-Sayed, M. A. Shape and size dependence of radiative, non-radiative and photothermal properties of gold nanocrystals. *Int. Rev. Phys. Chem.* **2000**, *19*, 409–453.
- (36) Chithrani, B. D.; Chan, W. C. W. Elucidating the mechanism of cellular uptake and removal of protein-coated gold nanoparticles of different sizes and shapes. *Nano Lett.* **2006**, *7*, 1542–1550.
- (37) Chithrani, B. D.; Ghazani, A. A.; Chan, W. C. W. Determining the size and shape dependence of gold nanoparticle uptake into mammalian cells. *Nano Lett.* **2006**, *6*, 662–668.
- (38) Leroueil, P. R.; Berry, S. A.; Duthie, K.; Han, G.; Rotello, V. M.; McNerny, D. Q.; Baker, J. R.; Orr, B. G.; Holl, M. M. B. Wide varieties of cationic nanoparticles induce defects in supported lipid bilayers. *Nano Lett.* **2008**, *8*, 420–424.
- (39) Nikoobakht, B.; El-Sayed, M. A. Preparation and growth mechanism of gold nanorods (NRs) using seed-mediated growth method. *Chem. Mater.* **2003**, *15*, 1957–1962.
- (40) Nikoobakht, B.; El-Sayed, M. A. Evidence for bilayer assembly of cationic surfactants on the surface of gold nanorods. *Langmuir* **2001**, *17*, 6368–6374.
- (41) Khan, S. A.; Singh, A. K.; Senapati, D.; Fan, Z.; Ray, P. C. Bio-conjugated popcorn shaped gold nanoparticles for targeted photothermal killing of multiple drug resistant *Salmonella* DT104. *J. Mater. Chem.* **2011**, *21*, 17705–17709.
- (42) Singh, A. K.; Lu, W.; Senapati, D.; Khan, S. A.; Fan, Z.; Senapati, T.; Demeritte, T.; Beqa, L.; Ray, P. C. Long-range nanoparticle surface-energy-transfer ruler for monitoring photothermal therapy response. *Small* **2011**, *7*, 2517–2525.
- (43) Berne, B. J.; Pecora, R. *Dynamic Light Scattering: with Applications to Chemistry, Biology, and Physics*; Dover Publications, Inc.: Mineola, NY, 1976, 2000; pp 114–157.
- (44) Tirado, M. M.; Garcia de la Torre, J. Rotational-dynamics of rigid, symmetric top macromolecules: Application to circular-cylinders. *J. Chem. Phys.* **1980**, *73*, 1986–1993.
- (45) Bosisio, C.; Quercioli, V.; Chirico, G.; D’Alfonso, L.; Bettati, S.; Raboni, S.; Campanini, B.; Collini, M. Effect of the point mutation H148G on GFPmut2 unfolding kinetics by fluorescence spectroscopy. *Biophys. Chem.* **2011**, *157*, 24–32.
- (46) Chirico, G.; Gardella, G. Photon correlation spectroscopy to 10 ns resolution. *Appl. Opt.* **1999**, *38*, 2059–2067.
- (47) Aragon, S. R.; Pecora, R. Fluorescence correlation spectroscopy and Brownian rotational diffusion. *Biopolymers* **1975**, *14*, 119–137.
- (48) Tsay, J. M.; Doose, S.; Weiss, S. Rotational and translational diffusion of peptide-coated CdSe/CdS/ZnS nanorods studied by fluorescence correlation spectroscopy. *J. Am. Chem. Soc.* **2006**, *128*, 1639–1647.
- (49) Haustein, E.; Schwille, P. Single-molecule spectroscopic methods. *Curr. Op. Struct. Biol.* **2004**, *14*, 531–540.

- (50) Berland, K. M.; So, P. T. C.; Chen, Y.; Mantulin, W. W.; Gratton, E. Scanning two-photon fluctuation correlation spectroscopy: particle counting measurements for detection of molecular aggregation. *Biophys. J.* **1996**, *71*, 410–420.
- (51) Caccia, M.; Sironi, L.; Collini, M.; Chirico, G.; Zanoni, I.; Granucci, F. Image filtering for two-photon deep imaging of lymph nodes. *Eur. Biophys. J.* **2008**, *37*, 979–987.
- (52) Magde, D.; Webb, W. W.; Elson, E. L. Fluorescence correlation spectroscopy III. Uniform translation and laminar flow. *Biopolymers* **1978**, *17*, 361–376.
- (53) Collini, M.; D'Alfonso, L.; Caccia, M.; Sironi, L.; Panzica, M.; Chirico, G.; Rivolta, I.; Lettieri, B.; Miserocchi, G. In vitro - in vivo fluctuation spectroscopies. In *Optical Fluorescence Microscopy*; Diaspro, A., Ed.; Springer Verlag: New York, 2011.
- (54) Jana, N. R.; Gearheart, L.; Murphy, C. J. Wet chemical synthesis of high aspect ratio cylindrical gold nanorods. *J. Phys. Chem. B* **2001**, *105*, 4065–4067.
- (55) Thierry, B.; Ng, J.; Krieg, T.; Griesser, H. J. A robust procedure for the functionalization of gold nanorods and noble metal nanoparticles. *Chem. Commun.* **2009**, *13*, 1724–1726.
- (56) Chirico, G.; Beretta, S.; Baldini, G. Conformation of interacting lysozyme by polarized and depolarized light scattering. *J. Chem. Phys.* **1999**, *110*, 2297–2304.
- (57) Biagioni, P.; Celebrano, M.; Savoini, M.; Grancini, G.; Brida, D.; Mátéfi-Tempfli, S.; Mátéfi –Tempfli, M.; Duò, L.; Hecht, B.; Cerullo, G.; et al. Dependence of the two-photon photoluminescence yield of gold nanostructures on the laser pulse duration. *Phys. Rev. B* **2009**, *80*, 45411.
- (58) Boyd, G. T.; Yu, Z. H.; Shen, Y. R. Photoinduced luminescence from the noble metals and its enhancement on roughened surfaces. *Phys. Rev. B* **1986**, *33*, 7923–7936.
- (59) Boyd, G. T.; Rasing, T.; Leite, J. R. R.; Shen, Y. R. Local-field enhancement on rough surfaces of metals, semimetals, and semiconductors with the use of optical second-harmonic generation. *Phys. Rev. B* **1984**, *30*, 519–526.
- (60) Chen, Y.; Mueller, J. D.; So, P. T. C.; Gratton, E. The Photon Counting Histogram in Fluorescence Fluctuation Spectroscopy. *Biophys. J.* **1999**, *77*, 553–567.
- (61) Alexis, F.; Pridgen, E.; Molnar, L. K.; Farokhzad, O. C. Factors affecting the clearance and biodistribution of polymeric nanoparticles. *Mol. Pharmacol.* **2008**, *5*, 505–515.
- (62) Van de Broek, B.; Devogdt, N.; D'Hollander, A.; Gijs, H.-L.; Jans, K.; Lagae, L.; Muyldermaans, S.; Maes, G.; Borghs, G. Specific cell targeting with nanobody conjugated branched gold nanoparticles for photothermal therapy. *ACS Nano* **2011**, *5*, 4319–4328.
- (63) Huff, T. B.; Hansen, M. N.; Zhao, Y.; Cheng, J.-X.; Wei, A. Controlling the cellular uptake of gold nanorods. *Langmuir* **2007**, *23*, 1596–1599.
- (64) Wachsmuth, M.; Waldeck, W.; Langowski, J. Anomalous diffusion of fluorescent probes inside living cell nuclei investigated by spatially resolved fluorescence correlation spectroscopy. *J. Mol. Biol.* **2000**, *298*, 677–689.
- (65) Rivolta, I.; Panariti, A.; Collini, M.; Lettieri, B.; D'Alfonso, L.; Sironi, L.; Miserocchi, G.; Chirico, G. A biophysical model of intracellular distribution and perinuclear accumulation of particulate matter. *Biophys. Chem.* **2011**, *158*, 134–140.
- (66) Klein, M. V.; Furtak, T. E., Eds. *Optics*; John Wiley & Sons: New York, 1985; pp 468–480.
- (67) Wohland, T.; Friedrich-Bénét, K.; Pick, H.; Preuss, A.; Hovius, R.; Vogel, H. The characterization of a transmembrane receptor protein by fluorescence correlation spectroscopy. In *Single Molecule Spectroscopy, Nobel Conference Lectures*; Rigler, R., Orrit, M., Basché, T., Eds.; Springer, Mineola, New York, 2001; pp 195–210.
- (68) Digman, M. A.; Dalal, R.; Horwitz, A. F.; Gratton, E. Mapping the Number of molecules and brightness in the laser scanning microscope. *Biophys. J.* **2008**, *94*, 2320–2332.
- (69) Malcai, O.; Lidar, D. A.; Biham, O.; Avnir, D. Scaling range and cutoffs in empirical fractals. *Phys. Rev. E* **1997**, *56*, 2817–2828.
- (70) Sironi, L.; Freddi, S.; D'Alfonso, L.; Collini, M.; Gorletta, T.; Soddu, S.; Chirico, G. p53 Detection by fluorescence lifetime on a hybrid fluorescein isothiocyanate gold nanosensor. *J. Biomed. Nanotechnol.* **2009**, *5*, 683–691.
- (71) Parker, W. C.; Chakraborty, N.; Vrakkis, R.; Elliott, G.; Smith, S.; Moyer, P. J. High-resolution intracellular viscosity measurement using time-dependent fluorescence anisotropy. *Opt. Expr.* **2010**, *18*, 16607–16617.
- (72) Eigen, M.; Rigler, R. Sorting single molecules: Application to diagnostics and evolutionary biotechnology. *Proc. Natl. Acad. Sci. U.S.A.* **1994**, *91*, 5740–5747.
- (73) Hu, Y.; Litwin, T.; Nagaraja, A. R.; Kwong, B.; Katz, J.; Watson, N.; Irvine, D. J. Cytosolic delivery of membrane-impermeable molecules in dendritic cells using pH-responsive core-shell nanoparticles. *Nano Lett.* **2007**, *7*, 3056–3064.
- (74) Tkachenko, A. G.; Xie, H.; Coleman, D.; Glomm, W.; Ryan, J.; Anderson, M. F.; Franzen, S.; Feldheim, D. L. Multifunctional gold nanoparticle-peptide complexes for nuclear targeting. *J. Am. Chem. Soc.* **2003**, *125*, 4700–4701.